ACS OMEGA

http://pubs.acs.org/journal/acsodf

Article

Effect of Corrosion Temperature on the Corrosion of Q235 Steel and 16Mn Steel in Sodium Aluminate Solutions

Bianli Quan, Junqi Li, and Chaoyi Chen*

Cite This: *ACS Omega* 2021, 6, 25904−25915

Read Online

ACCESS | Metrics & More | Article Recommendations

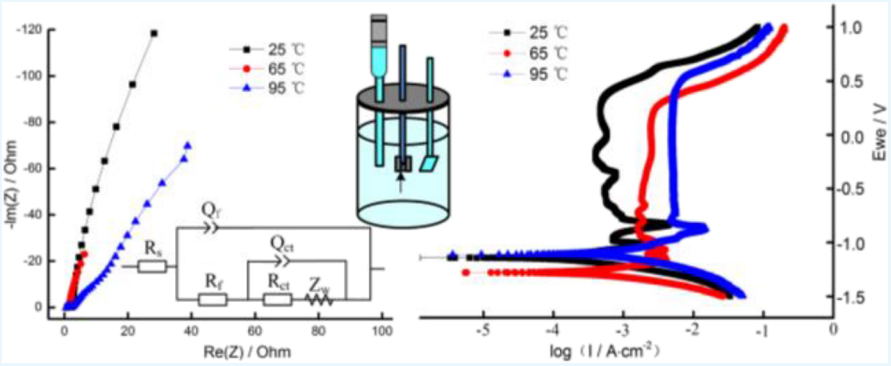

ABSTRACT: This study investigates the effect of corrosion temperature on the corrosion of Q235 steel and 16Mn steel in the sodium aluminate solution using the weight loss method and electrochemical method. The results indicate that the corrosion rates of two steels show an increasing trend with the temperature and that of Q235 steel increases more than that of 16Mn steel at higher temperatures. The corrosion products have changed from four forms at 25 °C to two forms at 65 and 110 °C, namely, the octahedral particles and the bulk particles formed by the flocculent aggregation. The corrosion products are composed of FeS, FeS_2, Fe_2O_3, Fe_3O_4, $NaFeO_2$, and Al_2O_3. The I_{corr} of the two steels increases with temperature, while R_p gradually decreases. The two steels are controlled by the charge transfer at 25 and 65 °C and the charge transfer and the ion diffusion at 95 °C, indicating that the temperature changes the kinetics of the corrosion process.

1. INTRODUCTION

High-sulfur bauxite is a general term for bauxite with the sulfur content of more than 0.7%.[1] High-sulfur bauxite is about 800 million tons in China, and the prospective reserve is about 2 billion tons,[2] but it has not yet been effectively used. The average alumina content is 68%, the aluminum-to-silicon ratio can reach 8, and the average sulfur content is 0.7% in high-sulfur bauxite, which is very suitable for the Bayer alumina production and has a high economic development value.[3,4] The study found that the sulfur of high-sulfur bauxite is mainly in the form of pyrite (FeS_2).[5] During the dissolution process of the Bayer production, S_2^{2-}, S^{2-}, and $S_2O_3^{2-}$ are mainly formed by 80% of pyrite reacting with alkali liquor.[3,6] These low-priced sulfur forms cause corrosion to equipment materials and other hazards to production processes.[7,8] At present, part of the dissolution equipment is made of stainless steel, while other tanks are mainly made of the traditional carbon steel in the production process of Bayer alumina in China.[9,10] With the recycling of alumina production, it is found that the steel has serious selective corrosion, pitting corrosion, corrosion cracking, and uniform corrosion.[11,12] In the production process of Bayer alumina, the different alumina production processes need to be completed at different temperatures, for example, the seed crystal decomposition temperature is 65 °C, the evaporation temperature is 110 °C, and the dilution temperature is 95 °C, approximately.[13] Therefore, the study of the corrosion behavior of corrosion temperature on the tank material is of great significance to material protection and material selection.

There are relatively few studied on the corrosion of steel in the sodium aluminate solution. Sriram and Tromans believed that the AlO_2^- ion in the sodium aluminate solutions have an inhibitory effect on the anodic dissolution of steel due to the formation of amorphous $Fe_{3-x}Al_xO_4$.[14] Xie and Chen indicated that the stability of the passive film on a low alloy steel surface is strongly affected by the temperature in Bayer liquid.[11] The

Received: April 27, 2021
Accepted: September 21, 2021
Published: September 28, 2021

https://doi.org/10.1021/acsomega.1c02220
ACS Omega 2021, 6, 25904−25915

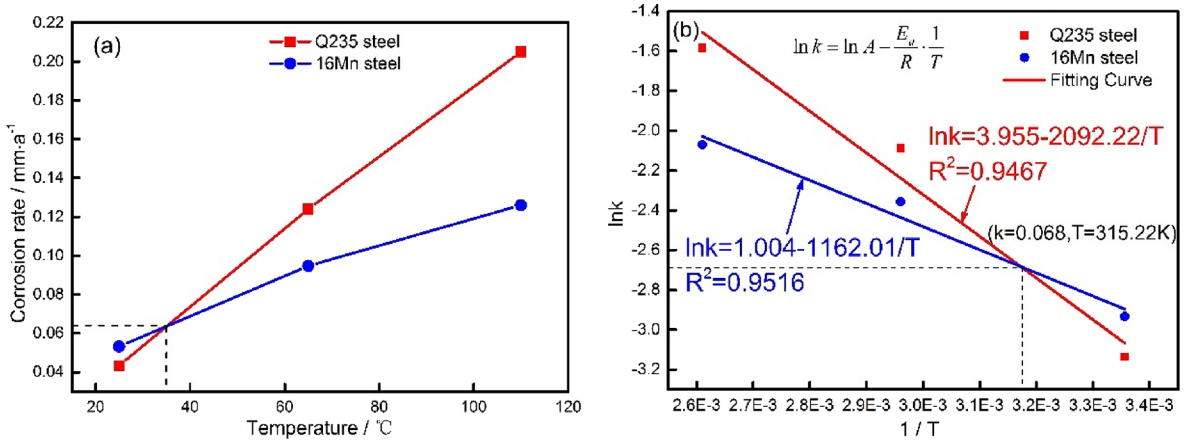

Figure 1. Relationship between the corrosion rate and temperature (a) and kinetic relationship (b) of two steels.

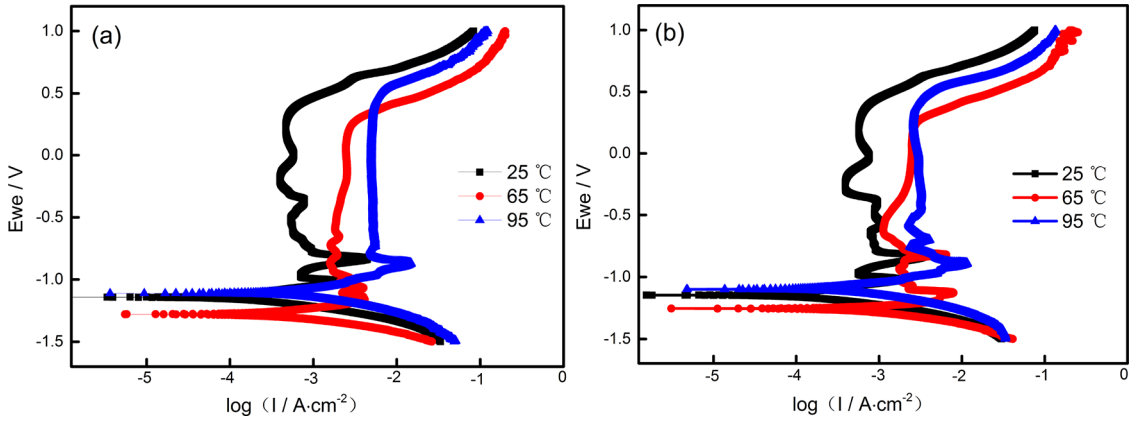

Figure 2. Potentiodynamic polarization curves of Q235 steel (a) and 16Mn steel (b) at different temperatures.

Table 1. Potentiodynamic Polarization Curves Fitting Results of Two Steels at Different Temperatures

working electrode	immersion temperature/°C	E_{corr}/V	I_{corr}/μA·cm^{-2}	β_a/mV	β_c/mV	R_p/Ω·cm^2	corrosion rate/mm·a^{-1}
Q235	25	−1.10	157.47	142.34	98.03	165.30	1.85
	65	−1.28	443.31	143.23	107.22	58.84	5.21
	95	−1.07	978.25	191.18	152.47	38.19	11.51
16Mn	25	−1.10	169.35	140.64	98.04	151.12	2.03
	65	−1.25	1417.00	216.61	155.43	29.43	16.67
	95	−1.06	1833.00	128.02	169.53	11.65	25.39

research results of Aydin et al. show that the open-circuit potential value of SnO_2-coated mild steel shifted toward more positive values compared to uncoated mild steel even under high elevated temperatures.[15] Mundhenk et al. testified that Fe-oxide formation is favored over $FeCO_3$ with moderately protective, thick, and porous characteristics toward higher temperatures.[16] Nimmervoll et al. revealed that the mass loss increased with rising temperature, and a model of the course of corrosion was proposed.[17] Adewumi et al. demonstrated that the corrosion rate increased as the exposure temperature, and uniform corrosion was noted on the specimens exposed to a low temperature (25 °C), while pitting corrosion was noted on those exposed to elevated temperature (55 °C).[18] The above literature discovered that the corrosion temperature has a great influence on the corrosion rate and corrosion mechanism. However, up to now, there are very little systematic reports on the influence of corrosion temperature on the corrosion of low carbon steel in sodium aluminate solutions in the literature. The morphology, composition, and dynamic characteristics of the corrosion products on the steel surface at different temperatures need to be resolved urgently.

In this paper, using the weight loss method and electrochemical method, combined with scanning electron microscopy (SEM), energy dispersive spectrometry (EDS), and X-ray powder diffraction (XRD) techniques, the influence of corrosion temperature on the corrosion behavior of Q235 steel and 16Mn steel was analyzed. The remaining parts of this paper are organized as follows. In Section 2, the experimental process is described. The experimental results are analyzed and discussed in accordance with three parts in Section 3: one is the corrosion rate, the other is the characteristics of the corrosion products, and another is the formation mechanism of the corrosion products. Finally, the conclusions are presented in Section 4. Its purpose is to systematically investigate the effect of corrosion temperature on the corrosion rate and corrosion mechanism of two steels and provide the theoretical basis for material protection of alumina production equipment.

https://doi.org/10.1021/acsomega.1c02220
ACS Omega 2021, 6, 25904−25915

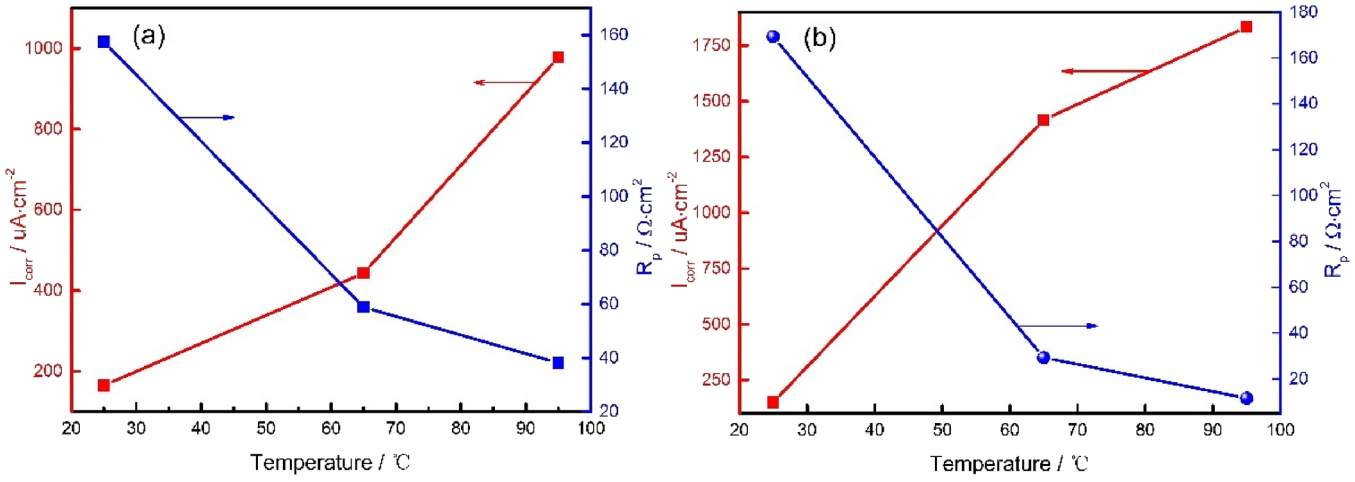

Figure 3. Evolution of I_{corr} and R_p for Q235 steel (a) and 16Mn steel (b) at different temperatures.

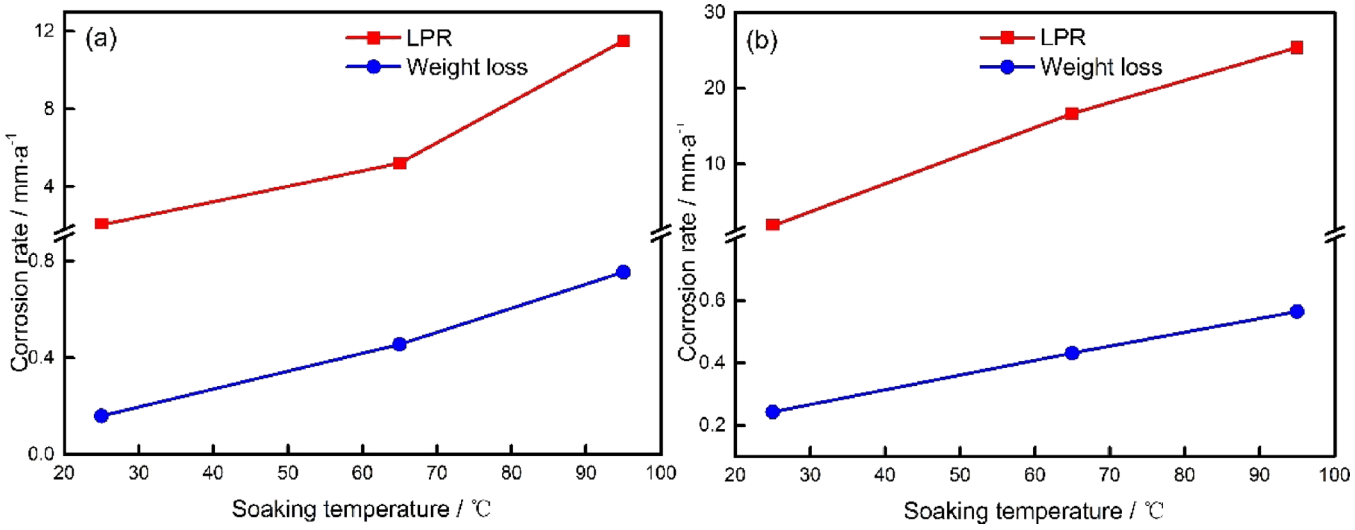

Figure 4. Comparison of the corrosion rates of Q235 steel (a) and 16Mn steel (b) obtained by the weight loss method and electrochemical method.

2. RESULTS AND DISCUSSION

2.1. Corrosion Rate. *2.1.1. Weight Loss Method.* The effect of corrosion temperature on the corrosion rate of Q235 steel and 16Mn steel is shown in Figure 1a. It can be seen that the corrosion rates of two steels increase with the increase in temperature. At the same time, it is also found that the corrosion rate of Q235 steel is larger than that of 16Mn steel at higher temperatures. The main reason for this phenomenon may be the difference in alloying elements of steels,[19] and on the other hand, it may be that the activation energies (E_a) of the corrosion reaction of two steels are different.[20] Because raising the temperature is beneficial to the reaction with greater activation energy, the reaction with low activation energy has less influence on the temperature.

To further analyze the corrosion kinetics of two steels, according to the Arrhenius equation $\ln k = \ln A - \frac{E_a}{R}\cdot\frac{1}{T}$, the linearization process of Figure 1a was carried out, and the result is shown in Figure 1b. From the linear relationship, the influence of corrosion temperature (T) on the reaction rate constant (k) was determined, and then the activation energies of the corrosion reactions for two steels were obtained. The corrosion kinetic equations of two steels are shown in eqs 1 and 2.[21]

$$\ln k_{(Q235)} = 3.955 - 2092.22 \times \frac{1}{T} \quad (1)$$

$$\ln k_{(16Mn)} = 1.004 - 1162.01 \times \frac{1}{T} \quad (2)$$

Compared with the Arrhenius equation, the E_a of corrosion reaction for Q235 steel is 17.39 kJ/mol, while that of 16Mn steel is 9.66 kJ/mol; it was found that E_a for Q235 steel is significantly greater than that of 16Mn steel. According to the law of the influence of activation energy on the reaction rate, the greater the activation energy, the more drastic the reaction rate changes with temperature, that is, increasing the temperature is more conducive to the reaction with high activation energy. Therefore, as the temperature rises, the corrosion rate of Q235 steel increases more than that of 16Mn steel.

2.1.2. Potentiodynamic Polarization Curves. The influence of immersion temperature on the potentiodynamic polarization curves of Q235 steel and 16Mn steel is shown in Figure 2. The potentiodynamic polarization curves at different temperatures

https://doi.org/10.1021/acsomega.1c02220
ACS Omega 2021, 6, 25904−25915

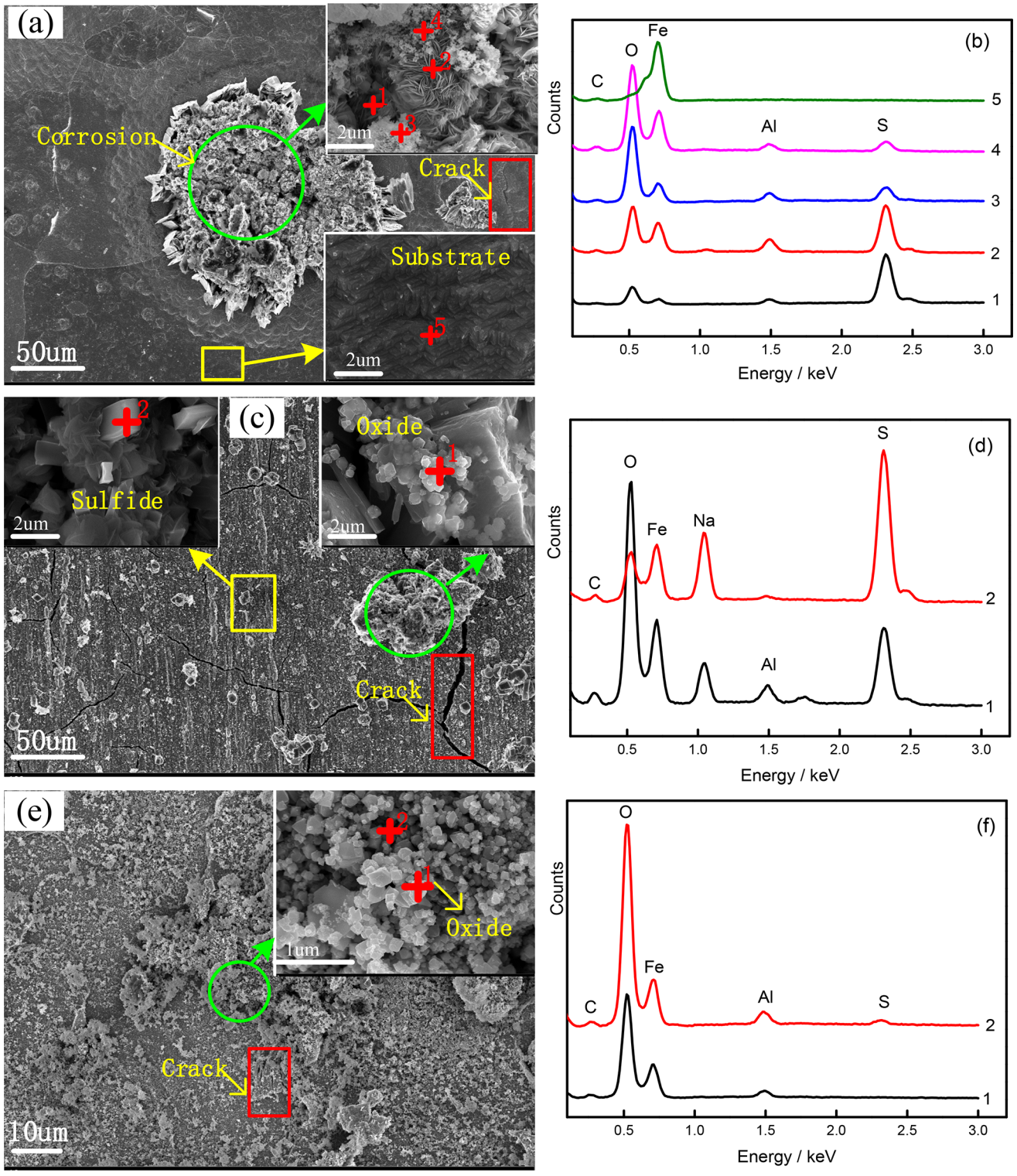

Figure 5. SEM morphologies (a, c, e) and EDS element analysis (b, d, f) of the corrosion products on the Q235 steel surface at different temperatures. (a, b) 25 °C; (c, d) 65 °C; (e, f) 110 °C.

are very similar, indicating that both Q235 steel and 16Mn steel have similar electrochemical behaviors. The cathodic reactions are the same, both are hydrogen evolution processes, taking into account the strong alkaline solution, and the anodic curves both show significant activation−passivation phenomena.

The acquisition of electrochemical parameters could provide more corrosion information.[22] Table 1 shows the corrosion potentials (E_{corr}), the polarization resistances (R_p), the anodic Tafel slope (β_a), the cathodic Tafel slope (β_c), the corrosion currents (I_{corr}), and the corrosion rate (R) obtained from the Tafel fitting of the potentiodynamic polarization curve data. It can be seen from the anode curve that the activation and dissolution trend of two steels is the same with temperature. The higher the temperature, the easier the corrosion will proceed from the thermodynamic analysis.[15]

https://doi.org/10.1021/acsomega.1c02220
ACS Omega 2021, 6, 25904−25915

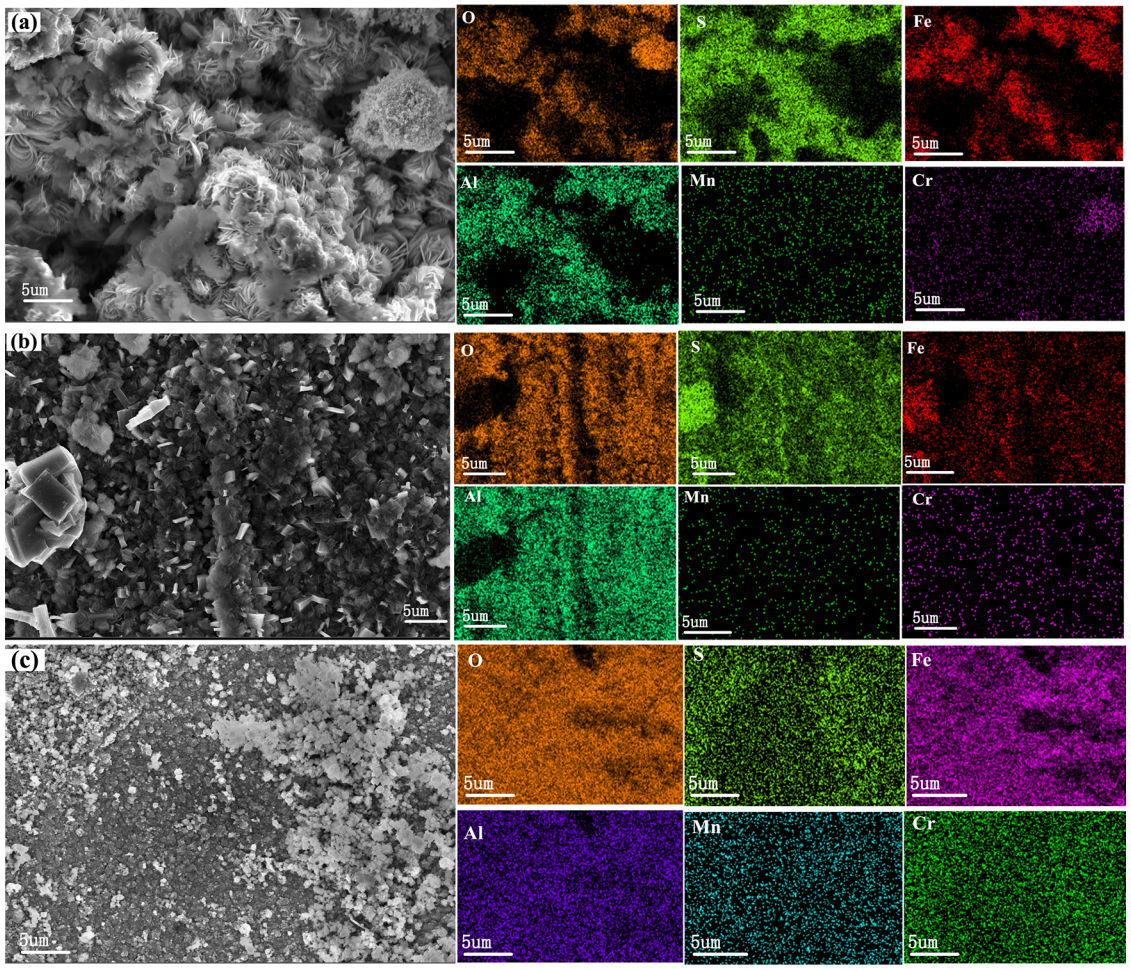

Figure 6. Morphologies and element distribution of the corrosion products on the Q235 steel surface at different temperatures. (a) 25 °C; (b) 65 °C; (c) 110 °C.

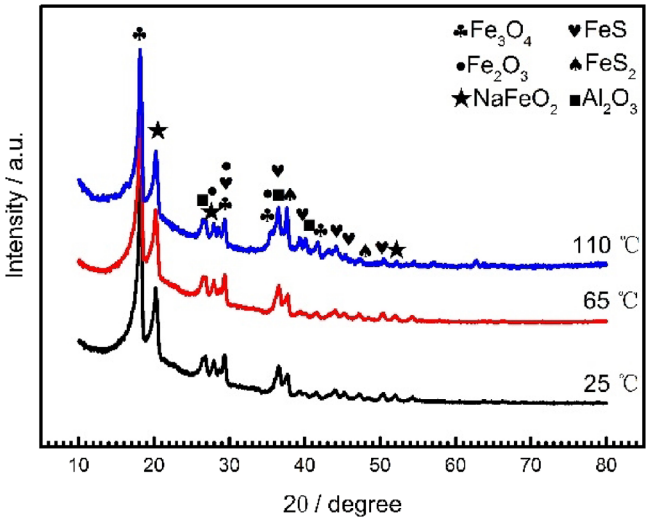

Figure 7. XRD analysis of the corrosion products on Q235 steel at different temperatures.

The changes in I_{corr} and R_p at different temperatures are shown in Figure 3. As can be seen in Table 1 and Figure 3, as the immersion temperature increases, the I_{corr} of two steels is gradually increased, while R_p decreases, so the corrosion rate also increases. Hence, the temperature is the driving force for ion diffusion, and the corrosion rate accelerates as the temperature rises.[23] This result shows that the corrosion rate obtained by the polarization curve is completely consistent with the result obtained by the weight loss method. By comparison, it is found that the corrosion rate of 16Mn steel is greater than that of Q235 steel, which is consistent with the results of the weight loss method at low temperatures. The reason may be the difference in the alloy elements in two steels.

2.1.3. Corrosion Rate Comparison. The corrosion rates of Q235 steel and 16Mn steel obtained by the weight loss method and electrochemical method were compared, and the results are shown in Figure 4. The corrosion rate obtained by the polarization curve method is relatively larger than that of the weight loss method, and the result is roughly 10 times that of the weight loss method, but the change trend of the corrosion rate obtained by the two methods is basically the same. Due to the accumulation of corrosion products on the steel surface, the corrosion rate measured by the polarization curve method is much greater than the actual corrosion rate, which can no longer accurately reflect the actual state of the steel in corrosive media. The change trend of corrosion rate is basically consistent with the result of the weight loss method. So, for harsh conditions, such as higher temperatures and longer times, the polarization curve method can be used to obtain the trend of corrosion rate.

https://doi.org/10.1021/acsomega.1c02220
ACS Omega 2021, 6, 25904−25915

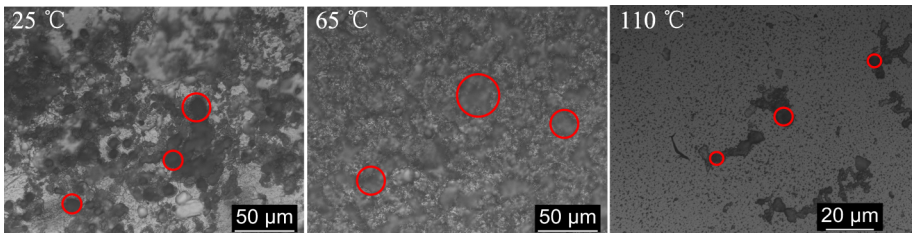

Figure 8. Surface morphologies of Q235 steels at different temperatures after the corrosion products are removed.

2.2. Characteristics of Surface Corrosion Products. *2.2.1. Morphology and Composition Analysis.* Figures 5 and 6 show the morphology and element distribution of the corrosion products on the Q235 steel surface at different temperatures. It can be seen that the corrosion products are mainly composed of four different forms of substances at 25 °C (Figure 5a). From the distribution of EDS elements (Figure 5b), they are mainly composed of four elements: Fe, O, S, and Al. The content of sulfur in different forms of corrosion products is completely different. One is the hydrangea-shaped corrosion products (Figure 6a) formed by flaky accumulation, which have a loose structure and relatively high sulfur content (position 2). As the corrosion progresses, the hydrangea-shaped corrosion products gradually grow up and accumulate, forming dense massive corrosion particles (position 1). Relatively speaking, their position is closer to the steel matrix, mainly composed of iron and sulfur, and the oxygen content is relatively small. Simultaneously, the corrosion products on the surface continue to react to form new compounds (positions 3 and 4), in which the content of oxygen is significantly increased, while the content of sulfur is relatively reduced. From the distribution of EDS elements in Figure 6a, the corrosion products are mainly composed of five elements (Fe, O, S, Al, and Na). At the same time, it is found that chromium is enriched in the corrosion layer, while manganese is evenly distributed in the corrosion products. Therefore, it is preliminarily judged that the loose sulfide generated at the initial stage will be transformed into a relatively dense and stable oxide (1 → 2 → 3 → 4), which will protect the matrix to a certain extent. At 25 °C, from the corresponding SEM morphology and EDS element analysis, it can be seen that the corrosion products are affected by the ions in the solution, which cause the corrosion products to fall off, exposing the similarly stacked steel matrix (position 5). Due to the low corrosion temperature, the corrosion of Q235 steel mainly occurs at carbon-enriched or surface defects, and small cracks are generated on the local surface.

The higher temperature provides a certain driving force for the formation of corrosive particles, and the rate of particle generation is relatively fast, so the particle size is relatively small. According to the thermodynamic analysis, the higher the temperature and the stronger the diffusion ability of ions, the easier it is to move between particles. When the corrosion temperature rises to 65 °C, the phenomenon of the engulfment between particles is more significant, and the faster the migration movement is, the smaller particles will gradually grow into larger coarse particles (Figures 5c and 6b). At the same time, the formed coarse particles further reduce the surface energy so that the steel surface is in a relatively stable and low free energy state. Therefore, for a certain amount of steel, the coarser the particles, the smaller the surface area, the lower the surface energy, and the lower the rate of particle generation. It can be seen from the morphology of 30,000 times that a large number of plate-like particles are deposited on the steel surface, so the degree of cracking on the steel surface is more serious (Figure 5c). There are two forms of corrosion products on the Q235 steel surface at 65 °C (Figure 5d): one is crystalline particles, which are composed of five elements (O, S, Fe, Na, and Al), and the other is a plate shape composed of three elements (Fe, S, and Na). According to the element distribution of EDS (Figure 6b), the plate-like particles are composed of iron and sulfur, which may be FeS and FeS_2. Therefore, the composition and morphology of corrosion products vary with temperature.[24] Sodium mainly comes from the sodium aluminate solution and participates in the corrosion reaction, which has a certain impact on the structure (density) of corrosion products.

When the temperature rises to 110 °C, the driving force of particle formation is greater, the particles continue to form, grow, and accumulate, the surface layer is more prominent, and the coverage of the corrosion products increases (Figure 6c). Due to the homogenization of the crystal particles on the steel surface,[25] the surface cracks are relatively small (Figure 5e). EDS analysis shows that the crystal particles are mainly composed of O, Fe, and Al elements, and there is almost no sulfur (Figure 5f).

2.2.2. XRD Analysis. The XRD analysis of corrosion products on the surface of Q235 steel at different temperatures is shown in Figure 7. It can be seen that the temperature has no effect on the composition of corrosion products but has a certain effect on the intensity of the diffraction peak, that is, it has a certain degree of the influence on the crystallinity of the particles. From the XRD diffraction peak intensity, the higher the corrosion temperature, the stronger the diffraction peak intensity, the better the crystallinity, and the better the crystal form. Using X-pert HighScore software to analyze the spectrum, it is found that the corrosion products are composed of FeS, FeS_2, Fe_2O_3, Fe_3O_4, $NaFeO_2$, and Al_2O_3.

2.2.3. Surface Corrosion Pit Depth. Figure 8 shows the surface morphology of Q235 steel after removing the corrosion products at different temperatures.

The surface morphologies of Q235 steels change greatly after cleaning the corrosion products at different temperatures. At 25 °C, the degree of surface etching is already very serious, the corrosion pits are more uniform and larger, and the surface is relatively uneven. At 65 °C, the surface etching phenomenon is evident, and there are fewer corrosion pits, but there are more striped corrosion marks on the surface, and the corrosion is more uniform. At 110 °C, a large number of small corrosion pits appear on the steel surface, but the local surface corrosion is more serious, and the corrosion pits are larger and deeper. Therefore, the higher the temperature, the greater the corrosion pit depth, and the greater the impact on the steel surface. This result is consistent with SEM.

https://doi.org/10.1021/acsomega.1c02220
ACS Omega 2021, 6, 25904−25915

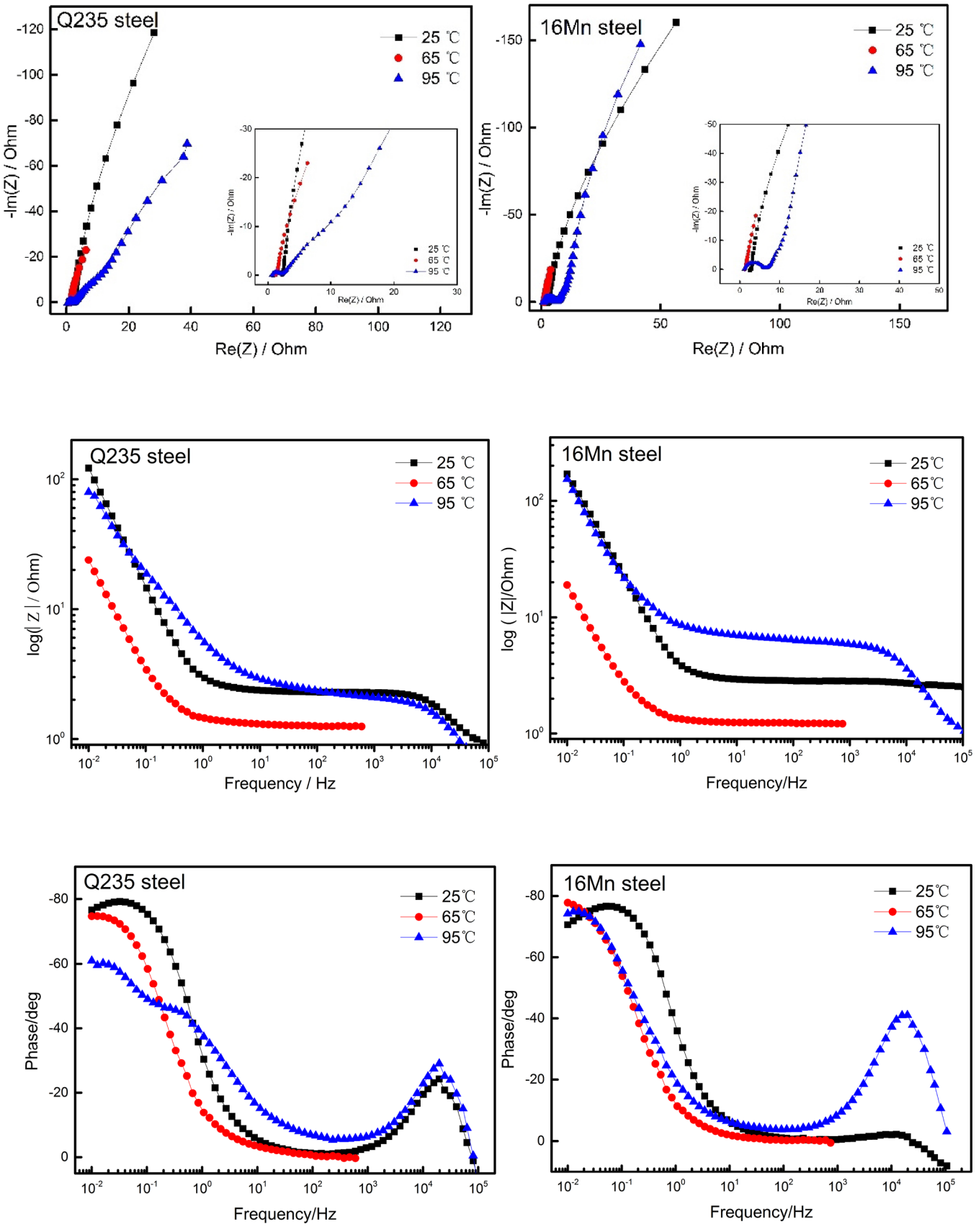

Figure 9. EIS of Q235 steel and 16Mn steel at different temperatures.

2.2.4. Electrochemical Impedance Spectroscopy. Figure 9 shows the EIS of Q235 steel and 16Mn steel at different temperatures. The overall trends of the Nyquist diagram and Bode diagram of two steels with the temperature are basically

https://doi.org/10.1021/acsomega.1c02220
ACS Omega 2021, 6, 25904−25915

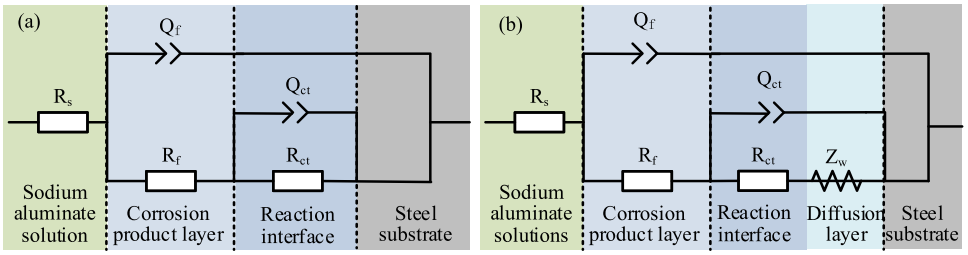

Figure 10. Equivalent circuits for the EIS of Q235 steel and 16Mn steel. (a) 25 and 65 °C; (b) 95 °C.

Table 2. Impedance Parameters Obtained from Q235 Steel and 16Mn Steel at Different Temperatures

	Q235 steel			16Mn steel		
parameters	25 °C	65 °C	95 °C	25 °C	65 °C	95 °C
$R_s/\Omega\cdot cm^2$	0.975	1.258	0.730	2.583	1.245	1.186
$R_f/\Omega\cdot cm^2$	1.336	0.234	1.420	0.266	4.933	4.829
$CPE_f(Y_0)/S^n\cdot\Omega^{-1}\cdot cm^{-2}$	2.20×10^{-5}	0.19	1.82×10^{-5}	3.48×10^{-4}	0.56	5.08×10^{-6}
n_1	0.94	0.92	0.96	0.85	0.92	0.99
$R_{ct}/\Omega\cdot cm^2$	1095	523.2	91.49	1027	415	2.087
$CPE_{ct}(Y_0)/S^n\cdot\Omega^{-1}\cdot cm^{-2}$	0.107	0.320	0.067	0.070	0.129	0.013
n_2	0.94	0.89	0.65	0.93	0.95	0.81
$W_R/\Omega\cdot cm^2$			0.025			0.019
W_T (10^{-4})			3.65			4.19
W_P			0.48			0.43
χ^2 (10^{-3})	1.27	0.77	5.39	3.53	4.21	7.05

the same. Judging from the Nyquist diagram and Bode diagram, it is composed of two overlapping semicircles at 25 and 65 °C, that is, there are two time constants (τ_{ct} and τ_f) (the double layer and the corrosion product layer). One is the Faraday process with intermediate frequency response, and the other is the corrosion product layer with high frequency response.[26] When the temperature reaches 95 °C, it is mainly composed of two semicircles and a straight line of 45°. Due to the increase in temperature, the ion diffusion speed is accelerated, and the corrosion products are dense enough, which hinders the diffusion of the substance to a certain extent. The impedance caused by the concentration polarization is relatively large. The entire corrosion is simultaneously controlled by the Faraday process, the corrosion product layer properties, and the ion diffusion, that is, the two time constants (τ_{ct} and τ_f) and the Warburg impedance.[27] It showed that the temperature changes, and the kinetics of the corrosion process has also changed.

Figure 9 is fitted with the aid of ZView fitting software according to the equivalent circuits of Figure 10.[28] The electrochemical parameters are listed in Table 3. Figure 10a[12] and Figure 10b[29] are employed to parse the electrochemical action of two steels at different temperatures. The reason for choosing two models is that there are two capacitive loops or two capacitive loops and a straight line of 45° in the EIS diagram.[26] In the first model (Figure 10a), the relaxation times at middle frequency (MF) and high frequency (HF) can be associated with the double layer and the corrosion product layer, respectively. In the second model (Figure 10b), the relaxation times at low frequency (LF), MF, and HF can be associated with the double layer, the presence of corrosion products, and ion diffusion, respectively. In the equivalent circuit, R_s is the solution resistance, R_f and Q_f (CPE_f) are the corrosion product layer resistance and capacitance, respectively, R_{ct} and Q_{dl} (CPE_{ct}) are the charge transfer resistance and dual-layer capacitance, respectively, and Z_w is the Warburg diffusion of ions. Since the corrosion product layer has defects and is not uniform, the capacitance is represented by Q.

In Table 2, n and Y_0 represent the exponent and admittance of the constant phase element (Q), respectively. The R_{ct} of two steels in the corrosion process gradually decreases with the increase in temperature. The R_{ct} of Q235 steel decreases from 1095 $\Omega\cdot cm^2$ at 25 °C to 91.49 $\Omega\cdot cm^2$ at 95 °C. The R_{ct} of 16Mn steel decreased from 1027 $\Omega\cdot cm^2$ at 25 °C to 2.087 $\Omega\cdot cm^2$ at 95 °C. It shows that as the temperature increases, the resistance to the electrochemical reaction of the two steels decreases, and the temperature has a significant influence on the electrochemical reaction. However, R_f is both much smaller than R_{ct} for two steels, and the change in temperature is also small. It indicates that the corrosion products are not very thick, especially the fact that the surface cracking degree is greater at low temperatures, and the temperature has an effect on the structure of the corrosion layer. Therefore, the corrosion process of two steels at 25 and 65 °C is mainly controlled by the charge transfer (activation energy), while that of two steels at 95 °C is simultaneously controlled by the charge transfer and the ion diffusion. At 95 °C, the W_R of the two steels is not much different, indicating that the corrosion products on the surface of the two steels have basically the same hindrance to ions. It was also found that the R_{ct} of Q235 steel is greater than that of 16Mn steel at different temperatures, which is consistent with the results of the potentiodynamic polarization curves.

2.3. Formation Mechanism of the Corrosion Products. The influence of corrosion temperature on the corrosion behavior of Q235 steel and 16Mn steel in sodium aluminate solution was studied by means of SEM-EDS, XRD, EIS, and polarization curve. The corrosion mechanism and the formation process of the corrosion products for Q235 steel and 16Mn steel were explored.

The cross-sectional scan results of 16Mn steel after 120 h exposure to the sodium aluminate solutions containing 4 $g\cdot L^{-1}$

https://doi.org/10.1021/acsomega.1c02220
ACS Omega 2021, 6, 25904−25915

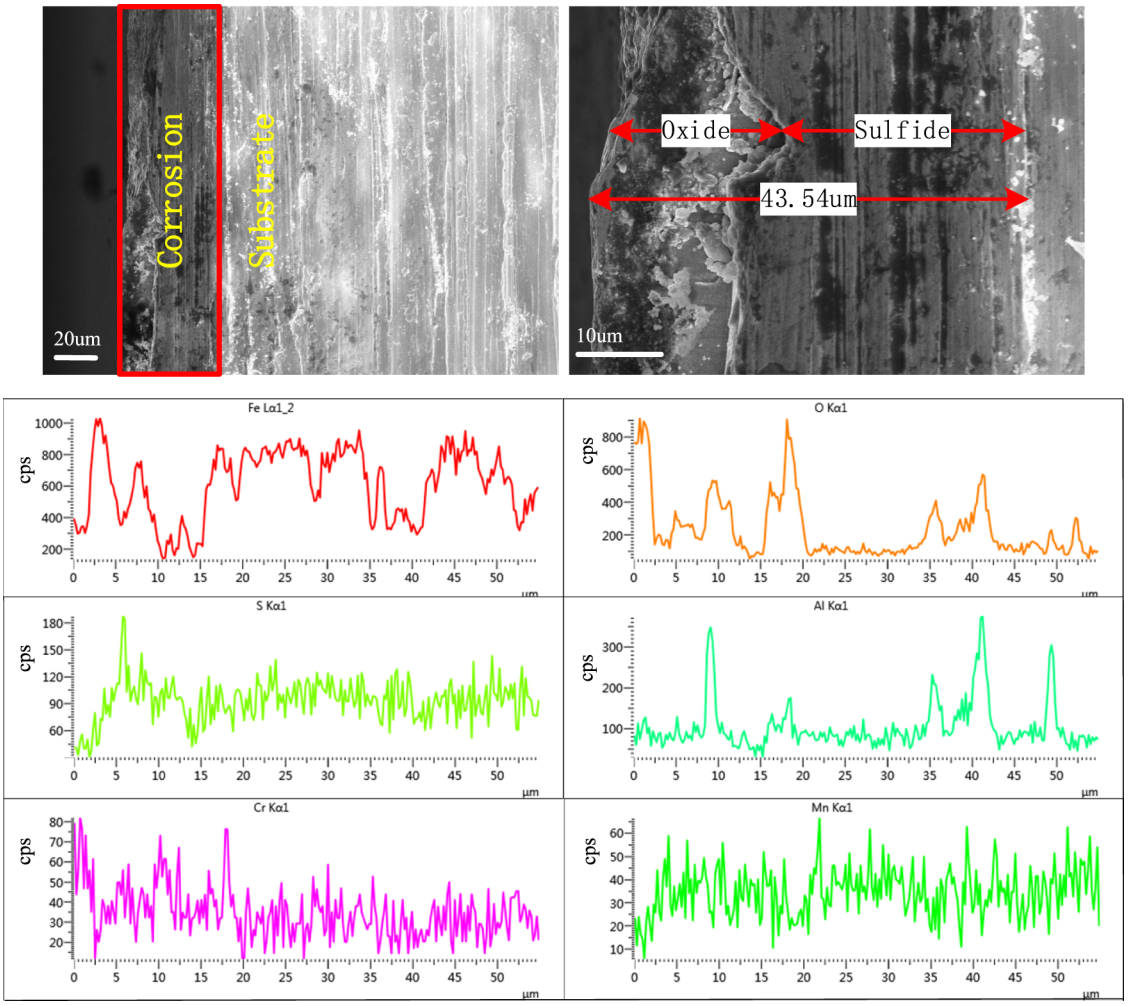

Figure 11. Cross-section scanning and EDS element analysis of 16Mn steels.

S^{2-} and 3 g·L^{-1} $S_2O_3^{2-}$ at 110 °C are shown in Figure 11. The thickness of the corrosion product reaches 43.54 μm. The line scan results showed that the content of Fe, O, S, and Al changes in different corrosion product layers, while chromium is enriched in the corrosion layer, but manganese is not enriched. Combined with the SEM and EDS analysis (Figure 12), it can be seen that S^{2-} is preferentially adsorbed to the steel surface and reacts to form iron sulfide (FeS and FeS_2). However, the formation of the corrosion products changes in the presence of S^{2-} and $S_2O_3^{2-}$, and the formed flocculent corrosion products (circle 1) at the initial stage of corrosion have higher sulfur content. As the corrosion progresses, the flocculent corrosion products aggregate to form a cluster substance (box 2), but the elemental composition has not changed from EDS analysis. As the corrosion continues, the structure and composition of the corrosion products have changed, and finally, the corrosion products of the octahedral crystal particles are formed on the surface of steels (cross 3), and sulfur in them almost disappears. The crystal particles can isolate the contact of corrosive ions with the steel substrate, so the steel surface is passivated. Combined with EDS elemental analysis, the formed flocculent corrosion products in the early stage of corrosion may be iron sulfide, and the corrosion products of the crystal particles in the later stage of corrosion may be iron oxide (Fe_3O_4).

3. CONCLUSIONS

The influence of corrosion temperature on the corrosion behavior of two steels in sodium aluminate solution was studied and discussed using SEM-EDS, XRD, EIS, and potentiodynamic polarization curve. The following main conclusions were obtained:

(1) The corrosion rates of Q235 steel and 16Mn steel show an increasing trend with the increase in temperature. The kinetic rate equations for two steels are determined by the weight loss method. Because the activation energies of the corrosion reaction of two steels are different, the corrosion rate of Q235 steel increases more than that of 16Mn steel at high temperatures.

(2) The corrosion products on the steel surface have changed from four forms at 25 °C to two forms at 65 and 110 °C, namely, the octahedral crystal particles and the bulk particles formed by flocculent aggregation. The corrosion products are composed of FeS, FeS_2, Fe_2O_3, Fe_3O_4, $NaFeO_2$, and Al_2O_3.

(3) Electrochemical results show that the I_{corr} of the two steels increases with temperature, while R_p gradually decreases. The corrosion process of two steels at 25 and 65 °C is mainly controlled by the charge transfer, while the corrosion process at 95 °C is simultaneously controlled by the charge transfer and the ion diffusion.

https://doi.org/10.1021/acsomega.1c02220
ACS Omega 2021, 6, 25904−25915

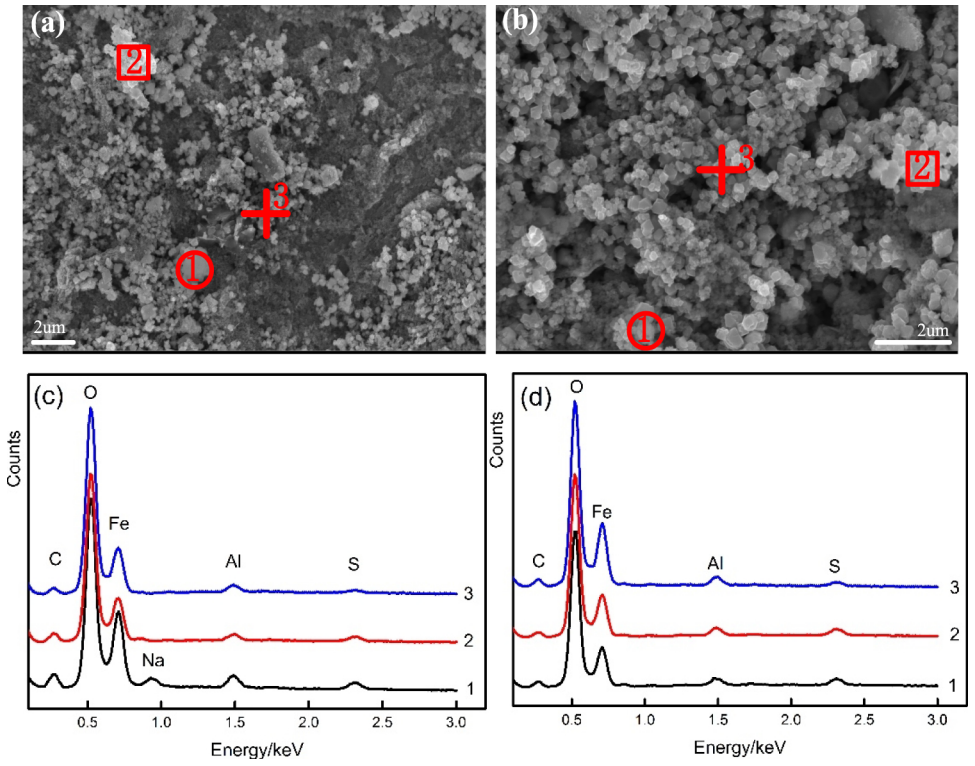

Figure 12. Evolution of the corrosion products and EDS element analysis on Q235 steel (a, c) and 16Mn steel (b, d).

The R_{ct} of Q235 steel is greater than that of 16Mn steel at different temperatures.

4. EXPERIMENTAL SECTION

4.1. Specimens and Solutions. The chemical compositions of Q235 steel and 16Mn steel in this study are listed in Table 3. The rectangular cubes with the sizes of 15 × 15 × 1 mm^3 and 20 × 10 × 1 mm^3 were cut from the Q235 steel and 16Mn steel, respectively. Surface preparation of the two steels was achieved by grinding up from 600 grit to 1800 grit with SiC abrasive paper, removing grease with acetone, cleaning with distilled water, and drying.

Table 3. Chemical Composition of Q235 Steel and 16Mn Steel (wt %)

sample	C	Si	Mn	Cr	P	S	Fe
Q235 steel	0.207	0.055	0.233	0.105	0.069	0.019	Bal
16Mn steel	0.178	0.290	1.645	0.041	0.056	0.017	Bal

The corrosion medium is composed of sodium aluminate solutions containing sulfur used to simulate sulfide ion concentration and alkali concentration in the evaporation processes. The sodium aluminate solutions contained 110 g·L^{-1} dissolved alumina (as Al_2O_3) and 255 g·L^{-1} NaOH and were prepared from high-purity chemicals and distilled water in a three-necked, round-bottom flask at 80−90 °C by magnetic stirring. Alumina ($Al_2O_3·3H_2O$) reacts with NaOH to form sodium aluminate ($NaAlO_2$) with the concentration of 110 g·L^{-1}.[30] Among them, 5 g·L^{-1} S^{2-} and 5 g·L^{-1} $S_2O_3^{2-}$ ions of the sodium aluminate solution were obtained by dissolving $Na_2S·9H_2O$ and $Na_2S_2O_3·5H_2O$. All chemicals used are of

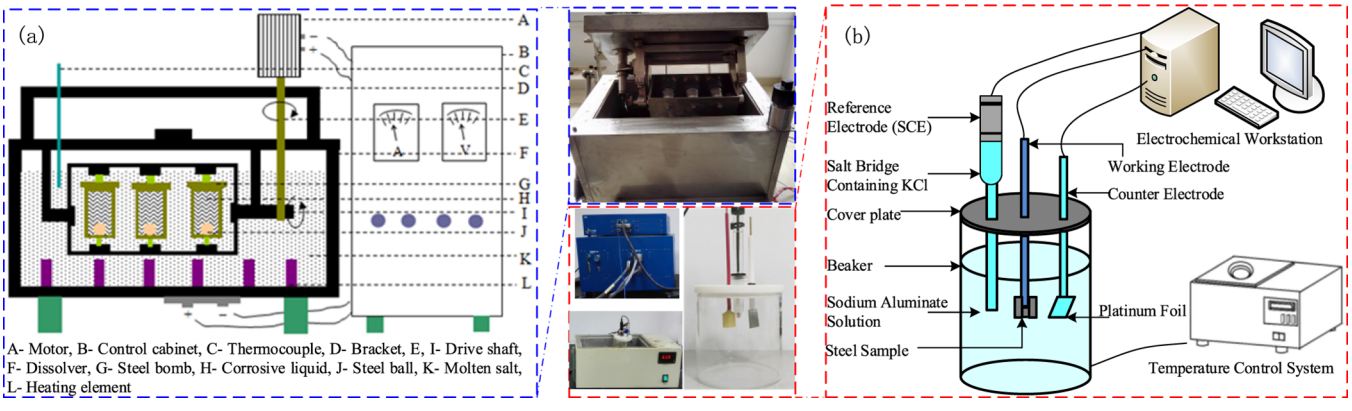

Figure 13. Schematic diagram of autoclave (a) and standard of electrochemical workstation (b).

https://doi.org/10.1021/acsomega.1c02220
ACS Omega 2021, 6, 25904−25915

analytical grade and come from Aladdin. The corrosion solutions were prepared and used at the time.

4.2. Weight Loss Experiments. The corrosion experiments were carried out at different temperatures (25, 65, and 110 °C) for 120 h in the autoclave (Figure 13a),[28] which are respectively the simulated normal temperature, the temperature of seed crystal decomposition, and the temperature of the evaporation process in the alumina production. Five Q235 steel coupons and 16Mn steel coupons were used in each experiment. Three steel coupons were used for the measurement of the weight change, while the other two were used to detect the morphology and the phase composition, respectively. Finally, the corrosion products were removed using 500 mL of distilled water, 500 mL of HCl, and 10 g of hexamethylenetetramine (GB/T 6074-1992). The corrosion rate (R) (mm·year^{-1} or mm·a^{-1}) was calculated using weight loss measurement, and the formula to calculate this is given as eq 3.[31]

$$R = 8.76 \times 10^4 \times (W_1 - W_2) \times (S \times t \times D)^{-1} \quad (3)$$

where R is the corrosion rate (mm·a^{-1}), W_1 is the quality of the sample before the corrosion test (g) with an accuracy of ±0.0001 g, W_2 is the corrosion sample after the removal of corrosion product quality (g) with an accuracy of ±0.0001 g, S is the sample surface area (cm^2) with an accuracy of 0.01cm^2, t is corrosion time (h) with an accuracy of 1 h, and D is the density of test steel (g/cm^3).

4.3. Corrosion Product Analysis. The morphology and composition of the corrosion products were observed with scanning electron microscopy (SEM, ZEISS SUPRA 40, Germany) with 10 kV acceleration voltage and energy dispersive spectroscopy (EDS, AZtec, Oxford, UK). The chemical composition of the corrosion products was analyzed by means of X-ray diffraction (XRD, X'pert Pro MPD Panalytical, Netherlands), with monochromated Cu-Ka radiation at the 2θ range of 10−80°. The software of HighScore Plus (Panalytical, Almelo, Netherlands) was selected to analyze the data. An optical microscope was used to measure the depth of corrosion pits on the steel surface after removing the surface corrosion products (DMI 5000M, Leica).

4.4. Electrochemical Tests. Electrochemical tests were carried out on an electrochemical workstation (Boi-Logic SAS, France) (Figure 13b)[28] with a conventional three-electrode polytetrafluoroethylene (PTFE) cell. The cell has been described elsewhere,[12,32] with the counter electrode made of platinum (CE) and a saturated calomel electrode (SCE) as a reference electrode and steel as a working electrode (WE) with the exposed areas of about 2.25 cm^2 (Q235 steel) and 2.00 cm^2 (16Mn steel). Before the electrochemical test, the WE values were immersed in a water bath for 120 h at different temperatures (25, 65, and 95 °C) in the corrosion medium. Since the SCE cannot withstand temperatures above 70 °C, the cells were placed in a water bath to achieve the test temperature of 65 °C.[22]

Electrochemical impedance spectroscopy (EIS) was carried out at the open-circuit potential (OCP) over the frequency from 10^5 Hz to 10^{-2} Hz, and the amplitude of the AC signal was 5 mV. All potentials reported in this paper were measured with respect to the SCE. The measured spectra were fitted by ZView software (3.0a) using the equivalent circuit (EC). To obtain the reproducibility of the data, the experiment was repeated. After, the polarization curve measurements were performed vs OCP from −1.50 to 1.00 V with a potential scan rate of 1 mV·s^{-1}. Both the cathodic and anodic branches were used to determine Tafel's extrapolation at the OCP.

AUTHOR INFORMATION

Corresponding Author

Chaoyi Chen − *College of Materials and Metallurgy, Guizhou University, Guiyang 550025, China; Guizhou Province Key Laboratory of Metallurgical Engineering and Process Energy Saving, Guiyang 550025, China*; Email: ccy197715@126.com

Authors

Bianli Quan − *College of Materials and Metallurgy, Guizhou University, Guiyang 550025, China; Guizhou Province Key Laboratory of Metallurgical Engineering and Process Energy Saving, Guiyang 550025, China*; orcid.org/0000-0002-6400-6386

Junqi Li − *College of Materials and Metallurgy, Guizhou University, Guiyang 550025, China; Guizhou Province Key Laboratory of Metallurgical Engineering and Process Energy Saving, Guiyang 550025, China*

Complete contact information is available at: https://pubs.acs.org/10.1021/acsomega.1c02220

Notes

The authors declare no competing financial interest.

ACKNOWLEDGMENTS

This work was supported by the National Natural Science Foundation of China (grant nos. U1812402, 52074096, and 51774102), Guizhou Province Outstanding Young Scientific and Technological Talent Training Plan ([2017]5626), Introduction Talent Fund Project of Guizhou University ([2019]43), and Guizhou University Cultivation Project ([2020]43).

REFERENCES

(1) Chai, W.; Huang, Y.; Peng, W.; Han, G.; Cao, Y.; Liu, J. Enhanced separation of pyrite from high-sulfur bauxite using 2-mercaptobenzimidazole as chelate collector: Flotation optimization and interaction mechanisms. *Miner. Eng.* **2018**, *129*, 93−101.

(2) Jin, H. X.; Wu, F. Z.; Li, J. Q.; Chen, C. Y.; Liu, H. L.; Yang, Q. Desulfurization of pyrite in high-sulfur bauxite with microwave roasting process. *J. Cent. South Univ. (Sci. Technol.)* **2020**, *51*, 2707−2718.

(3) Zhao, B.; Chen, Y.; Jiu, S. Effective Desulfurization and Alumina Digestion of High-Sulfur Bauxite by New Roasting Process with Conveying Bed. *Processes* **2021**, *9*, 390.

(4) Liu, Z.; Li, D.; Ma, W.; Yan, H.; Xie, K.; Zheng, L.; Li, P. Sulfur removal by adding aluminum in the bayer process of high-sulfur bauxite. *Miner. Eng.* **2018**, *119*, 76−81.

(5) Lou, Z.; Xiong, Y.; Feng, X.; Shan, W.; Zhai, Y. Study on the roasting and leaching behavior of high-sulfur bauxite using ammonium bisulfate. *Hydrometallurgy* **2016**, *165*, 306−311.

(6) Li, Z. Y. Study on the Flotation Desulfurization of High-sulfur Bauxite in Gansu. *Multi. Utili. Miner. Resour.* **2020**, *6*, 127−130.

(7) Zhou, X. J.; Yin, J.; Chen, Y. G.; Chen, Y. L.; Xia, W. T.; Xiang, X. Y.; Yuan, X. L. Simultaneous removal of sulfur and iron by the seed precipitation of digestion solution for high-sulfur bauxite. *Hydrometallurgy* **2018**, *181*, 7−15.

(8) Liu, Z. W.; Yan, H. W.; Ma, W. H.; Xie, K. W.; Li, D. Y.; Zheng, L. C.; Li, P. F. Sulfur Removal by Adding Iron During the Digestion Process of High-sulfur Bauxite. *Metall. Mater. Trans. B* **2018**, *49*, 509−513.

(9) Ye, L. M.; Wang, Y. M.; Yan, D. G.; Yang, C. Y. *Alumina production process and equipment*. Beijing: Metallurgical Industry Press: Bei Jing, 1987: pp. 134−361.
(10) Zhang, Y. f.; Chen, G. H.; Liu, J. S. Analysis of seven effect tubular falling film evaporate technology in alumina production. *Light Met.* **2015**, *03*, 19−23.
(11) Xie, Q.; Chen, W. Corrosion behavior of 16Mn low alloy steel in sulfide-containing Bayer solutions. *Corros. Sci.* **2014**, *86*, 252−260.
(12) Yuan, J. Y.; Chen, C. Y.; Li, J. Q.; Quan, B. L.; Lan, Y. P.; Wang, L. Z.; Fu, H.; Gai, J. X. Initial Corrosion Behavior of 12Cr1MoV Steel in Thiosulfate Containing Sodium Aluminate Solution. *Metals* **2020**, *10*, 1283.
(13) BI, S. *Alumina Production process*, 1nd ed. Chemical Industry Press: Beijing, 2006: pp. 32−37.
(14) Sriram, R.; Tromans, D. The Anodic Polarization Behaviour of Carbon Steel in Hot Caustic Aluminate Solutions. *Corros. Sci.* **1985**, *25*, 79−91.
(15) Ates, S.; Aydin, E. B.; Yazici, B. The corrosion behavior of the SnO2-coated mild steel in HCl solution at different temperature. *J. Adhes. Sci. Technol.* **2021**, *35*, 419−435.
(16) Mundhenk, N.; Carrero, S.; Knauss, K. G.; Wonneberger, R.; Undisz, A.; Wu, Y. Kinetic and thermodynamic analysis of high-temperature CO2 corrosion of carbon steel in simulated geothermal NaCl fluids. *Corros. Sci.* **2020**, *171*, 108597.
(17) Nimmervoll, M.; Schmid, A.; Mori, G.; Hönig, S.; Haubner, R. Surface sulphide formation on high-temperature corrosion resistant alloys in a H2S-HCl-CO2 mixed atmosphere. *Corros. Sci.* **2021**, *181*, 109241.
(18) Adewumi, A. A.; Maslehuddin, M.; Al-Dulaijan, S. U.; Shameem, M. Corrosion behaviour of carbon steel and corrosion resistant steel under elevated temperature and chloride concentration in simulated concrete pore solution. *Eur. J Environ. Civ. En.* **2021**, *25*, 452−467.
(19) Zuo, X.; Xiang, B.; Xing, L.; Wei, Z. Corrosion Behavior of 35CrMn and Q235 Steel in Simulated Acid Rain Conditions. *J. Mater. Eng. Perform.* **2012**, *21*, 524−529.
(20) Krieger, F.; Möglich, A.; Kiefhaber, T. Effect of proline and glycine residues on dynamics and barriers of loop formation in polypeptide chains. *J. Am. Chem. Soc.* **2005**, *127*, 3346−3352.
(21) Inica, V. Z. Significance and influence of the ambient temperature as a rate factor of steel reinforcement corrosion. *Bull. Mater. Sci.* **2002**, *25*, 375−379.
(22) Biancardia, O. V.; Rosaa, V. L.; Abreua, L. B.; Tavares, A. P. R.; Corrêa, R. G.; Cavalcanti, P. H.; Napoleão, B. I.; Pereira, D. S. E. Corrosion behavior of as-cast ZK60 alloy modified with rare earth addition in sodium sulfate medium. *Corros. Sci.* **2019**, *158*, 108092.
(23) Zhang, X.; Shyy, W.; Sastry, A. M. Numerical Simulation of Intercalation-Induced Stress in Li-Ion Battery Electrode Particles. *J. Electrochem. Soc.* **2007**, *154*, A910−A916.
(24) Sun, Q.; Chen, C.; Zhao, X.; Chi, H.; He, Y.; Li, Y.; Qi, Y.; Yu, H. Ion-selectivity of iron sulfides and their effect on H2S corrosion. *Corros. Sci.* **2019**, *158*, 108085.
(25) Bahmani, A.; Shin, K. S. Controlling the Microstructure and Texture Using Multidirectional Forging (MDF) to Develop a Low Corrosion Rate Mg Alloy. *Corrosion* **2020**, *76*, 750−765.
(26) Tang, S.; Dai, Z.; Tan, G.; Gong, S.; Liu, B.; Xie, G.; Peng, L.; Guo, J.; Li, Z. High-strength, ductility and corrosion-resistant in a novel Cu20Ni20Mn0.3Cr0.3Al alloy. *Mater. Chem. Phys.* **2020**, *252*, 123177.
(27) Virtanen, S. Electrochemical Theory, Corrosion. *Encyclopedia of Electrochemical Power Sources* **2009**, 56−63.
(28) Quan, B.; Li, J.; Chen, C. Effect of Corrosion Time on the Synergistic Corrosion of Q235 Steel in Sodium Aluminate Solutions. *Metals* **2021**, *11*, 753.
(29) Ayagou, M. D. D.; Tran, T. T. M.; Tribollet, B.; Kittel, J.; Sutter, E.; Ferrando, N.; Mendibide, C.; Thual, C. D. Electrochemical impedance spectroscopy of iron corrosion in H2S solutions. *Electrochim. Acta* **2018**, *282*, 775−783.
(30) Xie, Q. L.; Chen, W. M. Effect of S2- on corrosion behavior of low alloy steel in sodium aluminate solution. *Chin. J Nonferrous Met.* **2013**, *23*, 3462−3469.
(31) Quan, B. L.; Li, J. Q.; Chen, C. Y. Synergy Corrosion Effect of Thiosulfate and Sulfide on Q235 steel in Sodium Aluminate Solution. *Mater. Res. Express* **2019**, *6*, No. 025607.
(32) Khamseh, S.; Alibakhshi, E.; Ramezanzadeh, B.; Lecomte, J. S.; Laheurte, P.; Noirefalize, X.; Laoutid, F.; Vahabi, H. Tailoring hardness and electrochemical performance of TC4 coated Cu/a-C thin coating with introducing second metal Zr. *Corros. Sci.* **2020**, *172*, 108713.

https://doi.org/10.1021/acsomega.1c02220
ACS Omega 2021, 6, 25904−25915